Salcedo-Abraira, P.; Serrano Nieto, R.; Biglione, C.; Cabrero-Antonino, M.; Vilela, SM.; Babaryk, AA.; Tilve-Martínez, D.... (2023). Two Cu-Based Phosphonate Metal-Organic Frameworks as Efficient Water-Splitting Photocatalysts. Chemistry of Materials. 35(11):4211-4219. https://doi.org/10.1021/acs.chemmater.3c00054

Two Cu-based Phosphonate Metal-Organic Frameworks as Efficient Water Splitting Photocatalysts

Pablo Salcedo-Abraira[a§#], Rubén Serrano-Nieto[a§], Catalina Biglione[a], María Cabrero-Antonino[b], Sérgio M.F. Vilela[a], Artem A. Babaryk[a#], David Tilve-Martínez[a#], Antonio Rodriguez-Diéguez[c], Sergio Navalón[b], Hermenegildo García[b], Patricia Horcajada[a*]*

[a] IMDEA Energy Institute, Advanced Porous Materials Unit (APMU), Avda. Ramón de la Sagra 3, E-28935 Móstoles, Madrid, Spain.

[b] Departamento de Química and Instituto de Tecnología Química (CSIC-UPV), Universitat Politècnica de València, C/Camino de Vera s/n, 46022, Valencia, Spain

[c] Biochemistry and Electronics as Sensing Technologies group (BEST), Department of Inorganic Chemistry, University of Granada. Av. Fuentenueva s/n, 18071 Granada, Spain

*Email: patricia.horcajada@imdea.org

*Email: hgarcia@qim.upv.es

§P. S-A and R. S-N contributed equally to this paper

ABSTRACT

Two novel three-dimensional metal-organic frameworks (MOFs) based on the photoactive pyrene tetraphosphonate ligand and copper (denoted as IEF-8 & 9) have been hydrothermally synthesized and fully characterized (XRD, FTIR, TGA, SEM, XPS, etc.). Their crystal structures were unveiled by single-crystal X-ray diffraction. Remarkably, these materials exhibit coordinatively unsaturated copper (II) sites, free $–PO_3H_2$ and $–PO_3H$ acidic groups, and good thermal and chemical stability. Further, their optoelectronic characterization evidenced a photoresponse suitable for photocatalysis. In this sense, the photocatalytic activity of pyrene phosphonate MOFs was evaluated for the first time for the challenging hydrogen evolution reaction (HER). In particular, IEF-8 exhibited a catalytic efficiency higher than the benchmarked Ti carboxylate photocatalyst MIL-125(Ti)-NH_2, producing 1800 $\mu mol \cdot g^{-1}$ after 22 h under UV–Vis irradiation in absence of any co-catalyst. Furthermore, this material presented a good reusability (at least up to 4 cycles), preserving its activity and structural integrity.

INTRODUCTION

Although scarcely explored when compared with other metal organic frameworks (MOFs; phosphonate-MOFs *vs.* carboxylate-MOFs ≈ 1:10; according to Web of Science, September 2022), phosphonate-based MOFs (P-MOFs) present an extremely high scientific interest associated with: i) the versatility of metal bonding modes in the structure of P-MOFs caused by the multiple protonation states of the R-PO_3H_2 groups; ii) their capability to form stronger bonds with soft cations (*e.g.* divalent) compared to carboxylates due to their lower hard character (following the hard soft acid base theory, HSAB[1]), leading to chemically robust MOFs,[2-3] and iii) the formation of numerous non-covalent interactions (*e.g.* hydrogen bonds) inside their structures, resulting in

formation of P-MOFs with a high structural richness.[4] However, P-MOFs are difficult to synthesize and to be obtained as large crystals, hindering the determination of their crystal structure by conventional techniques.

Despite the limited number of P-MOFs, they have shown promising performances in a wide variety of applications (*e.g.* environment[5–9], biomedicine[10–12], catalysis[13–16] and energy[8,17–20]). Among these, P-MOFs can be considered as promising candidates for photocatalysis due to their structural robustness and the efficient charge separation.[21] These features can be exploited to produce H_2, a green energy vector, using renewable and clean solar energy[22] by hydrogen evolution reaction (HER). It is worthy commenting that nowadays hydrogen production from methane steam reforming is the main method of industrial hydrogen production and, therefore, the development of cost-effective and sustainable alternatives such as solar-driven photocatalytic HER is a technology of great interest.[23] Generally, the most efficient HER photocatalyst contain precious metals (*e.g.* platinum, palladium, rhodium) as they exhibit high catalytic efficiency[24]. Nevertheless, their scarcity and high cost limit their real practical application. Although other alternative to noble metals (*e.g.* transition metal oxides[25], sulphides[26] and phosphides[27]) have been proposed, they present a lower photocatalytic efficiency. Furthermore, MOFs are rich in topology, composition and highly dense in active sites. In addition, they can be extra and easy tunable through post-synthetic modifications focus on enhancing their photocatalytic properties.[28] In this sense, MOFs could be the next generation of catalysts since their versatility allows to optimize the catalytic performance.[29,30] Nevertheless, even when using photoactive MOFs, co-catalysts based on precious metals are often employed to reach competitive H_2 generation performances.[31]

Among the large number of MOF-based photocatalysts employed for the HER, some of the most active and stable materials for this purpose include traditional topologies such as MIL-125(Ti),

UiO-66(Zr) and MIL-101(Cr or Fe) as well as some porphyrin-based MOFs.[32] Recently, some of us have reported one of the first examples of P-MOFs as photocatalyst, namely $Ni(H_4ttbmp)(H_2O)_2]\cdot H_2O$ (H_4ttbmp: 2,4,6-tris[4-(phosphonomethyl)phenyl]-1,3,5-triazine), exhibiting an activity for the HER of 77 $\mu mol\cdot g^{-1}\cdot h^{-1}$.[15]

Since photoinduced ligand-to-metal electron transfer is one of the most common elementary steps involved in HER, the use of ligands based on highly conjugated organic molecules, able to absorb light in the solar spectrum is highly wanted. In this sense, pyrene-core ligands might be a suitable option to design P-MOFs with enhanced HER performance due to the distinctive photochemical properties of this chromophore. Pyrene is a highly symmetric condensed polycyclic aromatic hydrocarbon, that possesses unique characteristics such as visible light absorption, thermal stability, ability to donate electrons in its excited state and availability for coordination with metal ions when functionalized.[33] Until now and to the best of our knowledge, only three P-MOF structures have been so far reported employing pyrene phosphonate-based ligands and different cations (Ln^{3+}, Ba^{2+}, Ni^{2+})[34–36], but none of them have been tested as HER photocatalyst.

Therefore, for its use as photocatalyst, we designed a P-MOF with an appropriate combination of the metal-ligand properties based on the photoactive tetratopic phosphonate pyrene ligand (pyrene-1,3,6,8-tetrayltetrakis phosphonate) and the redox active Cu^{2+} ion to form robust and efficient photocatalytic P-MOFs. This combination could enhance visible light absorption by the pyrene chromophore and suppress electron-hole pair recombination by easily reducible Cu^{2+}. In this sense, the abundant, low cost and environmentally friendly copper cation is a well-known redox metal widely used as active site in photo- and/or electro-catalyst.[37] Thus, two novel copper-based P-MOF structures, named IEF-8 & 9 (IEF stands for IMDEA Energy Framework) were here successfully synthesized. Their crystal structures were unveiled by single-crystal X-ray diffraction,

fully characterizing both solids by different techniques (XRD, TGA, FTIR, SEM, XPS, etc.). While both solids demonstrated a high thermal and chemical stability, their in-deep optoelectronic characterization evidenced a photo-response suitable for photocatalysis. In accordance with this characterization IEF-8 and IEF-9 P-MOFs were evaluated as photocatalysts for the challenging HER under UV–Vis and simulated sunlight irradiation in absence of any co-catalyst, comparing the obtained results with other benchmarked photocatalysts (copper oxide, MIL-125(Ti)-NH_2[38], a Ni-based P-MOF[36], and other MOFs photocatalysts).

MATERIALS AND METHODS

Reagents. All the reagents were used as received without any purification: copper(II) nitrate trihydrate ($Cu(NO_3)_2 \cdot 3H_2O$ 99%, Acros Organics); nickel(II) nitrate hexahydrate ($Ni(NO_3)_2 \cdot 6H_2O$, 98%, Alfa Aesar); pyrene ($C_{16}H_{10}$, 98%, Sigma Aldrich); nitrobenzene ($C_6H_5NO_2$, 99%, Thermo Scientific); bromine (Br_2, ≥95,5%, Sigma Aldrich); tetrakis(triphenylphosphine)palladium(0) ([$Pd(PPh_3)_4$], 99%, Sigma Aldrich); triethyl phosphite ($P(OC_2H_5)_3$, 98%, Sigma Aldrich); petroleum ether (C_6H_{14}, ≥95%, LabKem); *n*-hexane (C_6H_{14}, technical grade, VWR Chemicals); hydrochloric acid (HCl, 37 %, Fisher Chemical); dichloromethane (CH_2Cl_2, 96 %, VWR Chemicals); methanol (CH_3OH, ≥99,9%, Chem-Lab); tetrahydrofuran (C_4H_8O, ≥99,9%, Chem-Lab); acetonitrile (C_2H_3N, ≥99,5%, Honeywell); N,N-dimethylformamide (C_3H_7NO, ≥99,5 %, Chem-Lab); octane (C_8H_{18}, ≥98%, Alfa Aesar); toluene (C_7H_8, 99,8%, LabKem)

Synthesis of IEF-8 $[Cu_2(Py(PO_3H)_4)(H_2O)_2]\cdot 4H_2O$. 0.196 g (0.81 mmol) of $Cu(NO_3)_2 \cdot 3H_2O$ and 0.211 g (0.405 mmol) of the lab-made linker $Py(PO_3H_2)_4$ (see SI) were dispersed in 27 mL of a mixture of distilled H_2O and MeOH (volumetric ratio 1:2) inside a 45 mL Teflon-lined autoclave. After that, the reactor was closed and heated at 120 °C from room temperature (RT) for 8 h and

then, maintained at this temperature for 48 h. After cooling to RT for 8 h, the obtained pale-yellow crystals were filtered and washed with water and methanol, recovered and dried under air. Yield: 40%

Synthesis of IEF-9 $[Cu_2(Py(PO_3H)_4)(H_2O)_2]\cdot 3H_2O$. 0.217 g (0.90 mmol) of $Cu(NO_3)_2\cdot 3H_2O$ and 0.336 g (0.45 mmol) of the home-made linker $Py(PO_3Et_2)_4$ (see SI) were dispersed in 30 mL of a mixture of distilled H_2O and MeOH (volumetric ratio 2:1) inside a 45 mL Teflon-lined autoclave. After that, 0.20 mL of HCl 6M were added to the reaction media. Finally, the reactor was closed and heated at 120 °C from RT in 8 h and then, maintained at this temperature for 48 h. After cooling to RT during 8 h, the obtained dark green crystals were washed with water and methanol, recovered and dried under air. Yield: 50%

Single-crystal X-ray diffraction. SC-XRD data of IEF-8 were collected on a Bruker D8 Venture diffractometer equipped with an air-cooled IμS Cu Kα microfocus source and Bruker Photon100 CMOS detector. IEF-9 data were collected on a Bruker APEX II CCD and Bruker D8 Venture with a Photon detector equipped with graphite monochromated MoKα radiation (λ = 0.71073 Å). The data reduction was performed with the APEX3 software, and corrected for absorption using SADABS. The crystalline structures were solved and refined by using the SHELX software package[39,40] and Olex2 software. Crystallographic data (excluding structure factors) for the structures reported in this paper have been deposited with the Cambridge Crystallographic Data Centre as supplementary publication nos. CCDC 2214087 and 2214398 for compounds IEF-8 and IEF-9, respectively. Copies of the data can be obtained free of charge on application to the Director, CCDC, 12 Union Road, Cambridge, CB2 1EZ, U.K. (Fax: +44-1223-335033; e-mail: deposit@ccdc.cam.ac.uk).

Powder X-ray diffraction. PXRD patterns were collected in an Empyrean Panalytical diffractometer, equipped with a PIXcel3D detector and with a copper radiation source (Cu Kα, λ =1.5406 Å), operating at 45 kV and 40 mA with 0.02 soller slits from 3 to 90 2θ° with an acquisition time of 120 s and refined using FullProf suit program.[41]

Variable temperature PXRD. VTPXRD data were collected on a D8 Advance Bruker AXS θ–2θ diffractometer (Cu Kα X-radiation, λ=1.54060 Å), equipped with a LYNXEYE XE detector, operating at 40 kV and 40 mA and an Anton Paar XRK 900 high-temperature chamber.

Scanning electron microscopy. SEM images were collected on a Hitachi TM-1000 microscope operating at 15 kV. Fourier transform infrared (FTIR) spectra were collected in the 4000 to 400 cm^{-1} range using a Thermo Nicolet 6700 FTIR instrument (Thermo Scientific, USA) with an ATR accessory. Elemental analyses were carried out in a Flash 2000 analyzer from Thermo Scientific.

Inductively coupled plasma optical emission spectroscopy. ICP-OES analyses were done in a 2300 DV spectrometer equipment from Perkin Elmer.

Thermo-gravimetric analyses. TGA were carried out using an SDT Q-600 thermobalance (TA instruments) in the 25-1000 °C range at 5 $°C \cdot min^{-1}$ and an airflow of 100 $mL \cdot min^{-1}$.

Diffuse reflectance UV-Vis measurements were recorded in a Perkin Elmer spectrometer (Lambda 19) equipped with an integrating sphere.

X-ray photoelectron spectra. XPS was recorded using a SPECS spectrometer equipped with an MCD-9 detector using a monochromatic Al (Kα = 1486.6 eV) X-ray source. CASA software has been used for the high-resolution XPS deconvolution. The XPS calibration is based on a series of independent measurements using Au, Ag and Cu foils. The Au 4f7/2, Ag 3d5/2 and Cu 2 p3/2 ISO standard binding energies for metallic gold, silver and copper used for calibration were 83.95, 368.22 and 932.63 eV, respectively.

Ultraviolet photoelectron spectroscopy. UPS measurements were carried out in a SPECS GmbH photoelectron spectroscopy analysis system equipped with a UHV system and an energy analyzer PHOIBOS 150 9MCD. He I (21.2 eV) was employed as photon source and with pass energy of 2 eV. The UPS instrument was calibrated by referring the Fermi level of Ag at 0 eV.

EPR measurements. EPR spectra were recorded at RT on a Bruker EMX-12 instrument operating in X band at 9.5 GHz, modulation amplitude of 1G and modulation frequency of 100KHz.

Photocatalytic tests. The photocatalytic HER experiments were carried out in water/methanol solutions. All the experiments were performed at least in triplicate and the presented data corresponds to the average values of the independent experiments. Briefly, the required amount of the photocatalyst (*i.e.* IEF-8 solid; 10 mg) was dispersed in 20 mL of a mixture of H_2O (16 mL) and methanol (4 mL), using a quartz reactor (51 mL), and the system sonicated for 20 min to obtain a good dispersion. Then, the system was purged with Ar for 1 h. The suspension under magnetic stirring was irradiated using a Hg-Xe lamp (150 W) equipped or not with an AM 1.5 filter to simulate the sunlight irradiation or visible light filter ($\lambda > 455$ nm).

The evolved gases from all experiments were analyzed by taking aliquots at different reaction times. The reaction aliquots were injected into an Agilent 490 Micro GC system (Molsieve 5 Å column using Ar as carrier gas). The temperature of the reactor was monitored and the pressure was analyzed using a manometer.

Photocatalytic $MV^{\bullet+}$ generation. The photocatalytic methyl viologen dication (MV^{2+}) reduction to methyl viologen radical cation ($MV^{\bullet+}$) solution was performed in acetonitrile using the IEF-8, IEF-9 and Ni-Pyrene P-MOF solids. Briefly, an acetonitrile suspension of the solids (0.2 $mg \cdot mL^{-1}$, 200 μL) was added to another acetonitrile solution of $MV(PF_6)_2$ (0.17 M, 1.05 mL)

and, then, additional acetonitrile (1.75 mL) was added to the quartz cuvette. Then, the solution was purged with Ar for 20 min. Subsequently, a Hg-Xe lamp (150 W) was employed for the irradiation, and the UV-Vis spectrum of the system was recorded periodically. The concentration of the $MV^{\bullet+}$ radical cation was calculated by applying the Lambert-Beer equation $A = \varepsilon \cdot l \cdot C$ where A is the absorbance measured at 390 nm, ε is the molar extinction coefficient of MV^{2+} at 390 nm (13900 $M^{-1} \cdot cm^{-1}$) and l is the length of the cell employed (1 cm).

Photocurrent measurements. Photocurrent measurements were performed in a three-electrode electrochemical setup. For this purpose, an Ag/AgCl electrode was employed as a reference electrode, a Pt electrode as a counter electrode, and a transparent fluoride-doped tin oxide (FTO)-coated glass with a thin layer of the IEF-8 solid as a working electrode. Before the measurements, the system was purged with Ar for 20 min to remove the oxygen present in the electrochemical cell. The current intensity was measured under both dark and under illumination with an optical fiber connected to a Hg-Xe lamp (150 W) by a series of consecutive 1 min periods of light off and on. The working FTO electrode was submitted to a polarization at potentials from 1.5 to -0.1 V.

RESULTS AND DISCUSSION

Synthesis and crystal structure of IEF-8 and IEF-9

Two novel 3D MOF structures based on Cu^{2+} and the pyrene-tetraphosphonate linker (home-made prepared at multi-gram scale, see experimental section at SI for further details), denoted as IEF-8 & IEF-9, were prepared optimizing the synthetic conditions (temperature, time, solvents, precursors, etc.) by using the very efficient high-throughput method.[42] One of the more relevant parameters to obtain the IEF-8 phase rather than IEF-9 one was the use of the acidic ligand instead of the ester-protected one. Interestingly, the different polarity of the linkers (and then, their solubility) made that the proportion of solvents used during the reactions (*i.e.* H_2O and MeOH)

could not be the same for both materials, changing from 1:2 for IEF-8 to 2:1 for IEF-9. As expected, the deprotection kinetics of both linkers might also play an important role in the reactivity. The use of the ester-protected linker required the addition of acid (*e.g.* HCl) to obtain well-crystallized materials instead amorphous powders. In contrast, the addition of an extra source of H^+ was not helpful when using the non-protected version of the linker, obtaining in this case amorphous powders.

Briefly, IEF-8 was obtained by solvothermal reaction of pyrene tetraphosphonic acid ($Py(PO_3H_2)_4$) and copper nitrate in a water:methanol mixture at 120 ºC during 64 h (see experimental section), obtaining pale yellow crystals and reaching yields of 40 %. The obtained crystals (~100 μm, Figure S1) were suitable for structure solution by SC-XRD. Hence, IEF-8 crystallized in the monoclinic space group *C*2/*c* (Table S1) with the formula $[Cu_2(Py(PO_3H)_4(H_2O)_2]\cdot 4H_2O$. The structure (Figure 1a) was built-up from CuO_5 square pyramids distorted in one of the corners of the pyramid base as secondary building unit (SBUs, Figure S2). The Cu, which was located in the base of the pyramid, and not inside, presented a coordination constituted by 4 different $–PO_3H$ groups coming from different linkers and by one slightly disorder water molecule in the distorted corner. Each phosphonic group from the ligand was coordinated to two different Cu atoms, maintaining one free –OH group and creating 1D zig-zag Cu-PO_3 chains along the *b* axis (Figure 1b). Perpendicular to these 1D chains, the structure presented void cavities (with a crystallographic size of ~8.5x5.5x6 Å) interconnected by small free spaces (~2.5 Å). The free water molecules of the structure (12 *per* unit cell) were located inside those cavities.

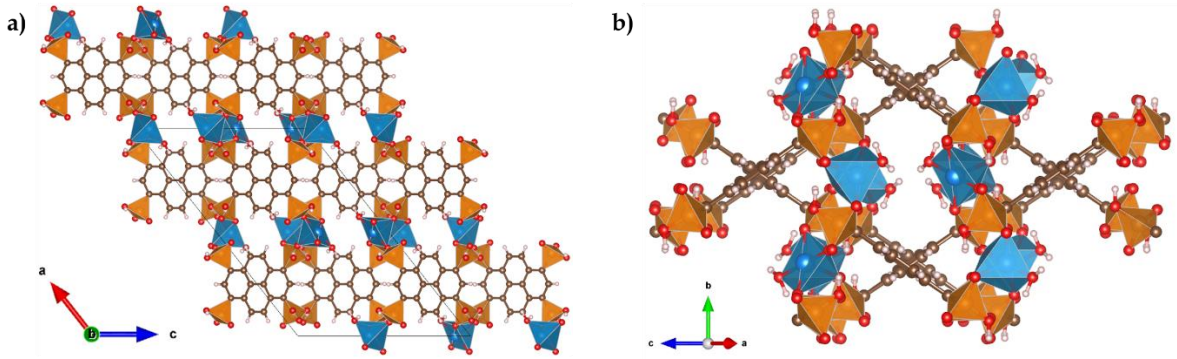

Figure 1. Crystalline structure of IEF-8 viewed from two different perspectives (a, b). Cu, C, O, P and H are represented in blue polyhedra, brown, red, orange polyhedral and white, respectively. Free water molecules were removed for clarity.

Similarly, IEF-9 was prepared using an analogous procedure, but using the ethyl ester-form of the linker (tetraphosphonic pyrene ethyl ester, $Py(PO_3Et_2)_4$) and copper nitrate in a solution of water/methanol/hydrochloric acid at 120 ºC during 64 h (see experimental section), yielding dark green crystals (yields ~50 %). These large crystals (~300 µm, Figure S3) were suitable for their structural resolution by SC-XRD. IEF-9 crystallizes in the monoclinic space group *C*2/*c* (Table S2) with the formula $[Cu_2(Py(PO_3H)_4(H_2O)_2]\cdot 3H_2O$. The structure (Figure 2a) was built up from CuO_6 octahedral sharing the apical corners with a CuO_4 square planar, creating Cu-O chains as SBUs (Figure S4) that were interconnected by the linkers. Interestingly, this SBU was described here for first time, being the Cu usually in two coordination geometries.

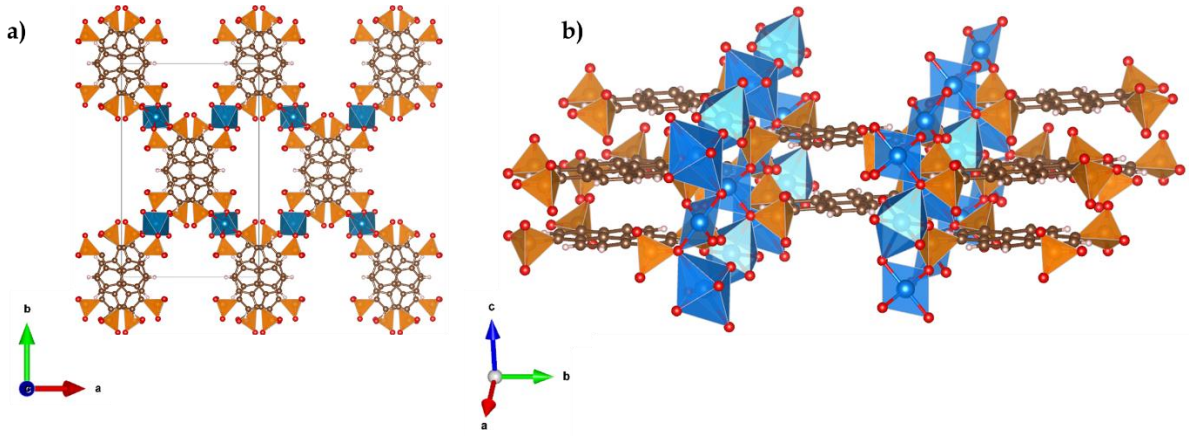

Figure 2. Crystalline structure of IEF-9 along two different perspectives (a, b). Cu, C, O, P and H are represented in blue polyhedra, brown, red, orange polyhedral and white, respectively. Free water molecules were removed for clarity.

As shown in Figure 2b, the Cu-O interconnected chains along the *a* axis direction presented the same octahedral-square order, but with different orientation of the polyhedra between chains (presenting a difference of tilting of 59.04°). On the other hand, the interconnected chains along the *b* axis presented different octahedral-square order, but with the same orientation of the polyhedra. The linkers exhibit an ABA stacking along the *c* axis (see Figure S5) with a 37.5° difference between them, derived from the different disposition of the Cu-O chains. The coordination sphere of the CuO_6 octahedral was composed by 4 O coming from 4 different phosphonate groups (two of them shared with the square planar) and by 2 O of the two coordinated water molecules. The Cu-O distances corresponding to the shared O (2.515 Å) are significantly larger than the other ones (2.027 and 1.901 Å), as a consequence of the Jahn-Teller effect.[43] The coordination sphere of the square planes is composed by 4 O coming from four different phosphonate groups. Each phosphonate group of the ligand is coordinated by two Cu atoms, being two of them bounded by the same O atom and the other two by two different O atoms, keeping

one free -OH group each. The structure discloses a frame of 1D channels along the *c* axis (~6x9 Å), where free water molecules are located (12 *per* unit cell).

Physicochemical characterization

The purity of these polycrystalline materials was corroborated by PXRD using Le Bail profile fittings (Figures S6, S7 and Tables S3, S4). FTIR spectra showed a significant shift of the phosphonate bands (ν P=O and ν P-O) of IEF-8 and IEF-9 when compared with the free linker (from 1006 to 1017 cm^{-1}, from 1076 to 1091 cm^{-1} and from 1132 to 1123 cm^{-1} for the IEF-8; and from 1009 to 1017 cm^{-1} and from 1068 to 1091 cm^{-1} for the IEF-9; Figures S8 and S9 respectively), supporting the coordination of the phosphonate groups to the Cu cations.

The chemical formula of IEF-8 $[Cu_2(Py(PO_3H)_4(H_2O)_2]\cdot 4H_2O)$ and IEF-9 ($[Cu_2(Py(PO_3H)_4(H_2O)_2]\cdot 3H_2O$) were confirmed by elemental analysis (C, H) and ICP-OES (P, Cu) in the dried solids, being the oxygen estimated by difference (%Exp.±S.D. (%Theo.) IEF-8: C 27.31±0.06 (25.51); H 2.47±0.04 (2.94); O 35.82 (38.22); P 17.9±0.9 (16.4); Cu 16.5±0.8 (16.8); and IEF-9: C 26.14±0.11 (26.13); H 2.79±0.08 (2.74); O 33.67 (36.98); P 16.9±0.8 (16.8); Cu 17.4±0.9 (17.3). On the other hand, although the estimation of the final composition is not possible by TGA due to the incomplete combustion of both solids in TGA analysis, the coordinated and free water contents were confirmed in both cases. Thus, TGA curve of the IEF-8 (Figure S10) showed an initial weight loss (from RT to 180 ºC) of approx. 8.3%, which corresponds with the departure of the 4 water molecules inside the pores of the structure. Then, a second weight loss appears (4.1%, from 200 to 300 ºC), which might correspond with the removal of the 2 coordinated water molecules. A last weight loss can be observed at around 550 ºC, corresponding with the combustion of the organic ligand. These data agree with the VT-PXRD patterns (Figure S11), where slight structural changes are observed with the departure of the 4 hydration water molecules

in the range 130-140 ºC, followed by a structural collapse at around 280 ºC when the last 2 coordinated water molecules are removed. Concerning the IEF-9, the TGA curve (Figure S12) shows an initial weight loss (from RT to 100 ºC) of approx. 7.5 %, which corresponds with the removal of the 3 free water molecules located within the pores. Then, a second loss of 5% (from 100 to 290 ºC) is observed, explained by the departure of the 2 coordinated water molecules. Finally, a weight loss at around 580 ºC is attributed to the ligand degradation. In this line, an initial phase transition can be observed in the range between 60-90 ºC in the VT-PXRD patterns (Figure S13), followed by the complete loss of crystallinity at 250 ºC. On the whole, IEF-8 exhibits a higher thermal stability than IEF-9 (structural transition 140 *vs.* 90 ºC; complete amorphization 280 *vs*. 250 ºC). Note here that the phase transitions evidenced in both solids might be the reason of the negligible gas sorption capacity determined upon the N_2 sorption experiments at 77 K, in spite of the crystallographic porosity of the pristine structures (8.5×5.5×6 Å and 6×9 Å for IEF-8 and IEF-9 respectively, see above).

Besides their thermal stability, the chemical robustness of both MOFs was assessed by suspending the powdered solids overnight in different organic solvents of industrial interest and commonly used in relevant catalytic reactions (see SI for further details), being their structural integrity evaluated by PXRD. Again, IEF-8 evidenced a higher stability than IEF-9 (Figures S14 and S15) in all the tested organic solvents (*i.e. N,N'*-dimethylformamide, acetonitrile, toluene, hexane, dichloromethane, methanol, octane and tetrahydrofurane). Notably, the structural integrity of both MOFs was kept also under water:methanol mixtures (conditions used in the HER) and in high relative humidity (RH) atmospheres (Figures S16 and S17), opening the gate to their use as hydrogen generation photocatalysts.

Optoelectronic characterization

Envisioning the potential of these materials as photocatalysts, their optoelectronic properties were investigated. Considering some similarities of the present two P-MOFs with an already reported nickel pyrene tetraphosphonate (*i.e.* same linker, free –OH groups, presence of coordinated and free water molecules),[36] this Ni Pyrene P-MOF was also prepared for comparison. Note here the successful scale-up of the synthesis (3 *vs.* 30 mL reaction), prepared at lower temperature (120 *vs.* 150 ºC) and slightly shorter times (72 *vs.* 60 h) with higher reactions yields (46 *vs.* 70 %) in absence of dangerous reactants (*i.e.* HF; see SI for further details). The stability of the Ni Pyrene P-MOF was also characterized, evidencing a higher thermal stability than IEF-8 & -9 (320 *vs.* 150 & 100 ºC) and similar chemical robustness in the selected solvents (see Figures S18-S22).

Then, IEF-8, IEF-9 and Ni-Pyrene P-MOF were characterized by XPS (Figures S23-S25). In general, the three MOFs exhibited some similarities due to the presence in their structure of pyrene tetraphosphonate as organic ligand. The C 1s spectrum showed the presence of the C-C sp^2 (284.4 eV) accompanied by the C-P (287 eV). In addition, the broad O 1s signal was centered at about 531.5 eV due to the presence of oxygen atoms coming from the $–PO^{3-}$ functional groups and Cu-O nodes for IEF-8 & 9 or Ni-O metal nodes for Ni-Pyrene P-MOF. The P 2p spectrum showed a band centered at 133 eV, attributed to the $–PO^{3-}$ functional group. IEF-8 and IEF-9 solids were characterized by a Cu 2p spectrum having the expected double peaks centered at 935 and 955 eV, corresponding to the Cu^{2+} $2p^{3/2}$ and Cu^{2+} $2p^{1/2}$ species, respectively.[44] Ni-Pyrene P-MOF exhibited a Ni 2p spectrum having double peaks at 856 and 874 eV, assigned to Ni^{2+} $2p_{3/2}$ and Ni^{2+} $2p_{1/2}$ species.

Furthermore, the optical properties of the novel Cu-based solids and the Ni-Pyrene P-MOF were evaluated by UV-Vis diffuse reflectance spectroscopy (Figure S26). All these MOFs exhibited a broad band with absorption edges up to about 450 nm in a similar way that the pyrene-tetraphosphonate molecule, employed as ligand. The optical band gaps of IEF-8 and IEF-9, or Ni-Pyrene P-MOF were estimated from these data using the Tauc plot (Figure S26; 2.73, 2.53 and 2.70 eV, respectively), whereas the valence band maxima versus the Fermi level (E^f_υ) were determined by XPS (Figure S27; 2.2, 2.6 and 2.4 eV, respectively). The valence band position with respect to the NHE (E_υ^{NHE}; Normal Hydrogen Electrode potential) was obtained from the equation $E_\upsilon^{NHE} = E_\upsilon^{f} + \phi_{sp} + E_0^{SHE}$ (Eq. 1) where ϕ_{sp} is the work function of the spectrometer (4.244 eV) and E_0^{SHE} is the energy of the SHE (Standard Hydrogen Electrode) with respect to vacuum level of the electron (−4.44 eV).[45] From this E_υ^{NHE} value and the optical band gap of the conduction band energy minimum (E_c^{NHE}) of the MOFs can be also determined.[46,47] As it can be observed in Figure 3, the three tested MOFs exhibit an appropriated band alignment, compatible to perform the HER in the presence of methanol as sacrificial electron donor. For the most active IEF-8 sample the valence band versus the Fermi level (E^f_υ) was also estimated by means of UPS with the value of 2.13 eV (Figure S28). Then, the E_υ^{NHE} was obtained from Eq. 1 with the value of 2.06 eV, in this case ϕ_{sp} of the UPS spectrometer is 4.37 eV. Additionally, valence band maximum of IEF-8 estimated by subtracting the UPS spectrum width (Figure S28) from the He I energy (21.22 eV) source and referred to the SHE resulted to be 1.95 V. Importantly, both XPS and UPS measurements have led to almost equal valence band values. Moreover, the UPS spectrum was recorded also with a negative applied voltage without observing change in the shape of the spectrum and reconfirming the valence band potential.

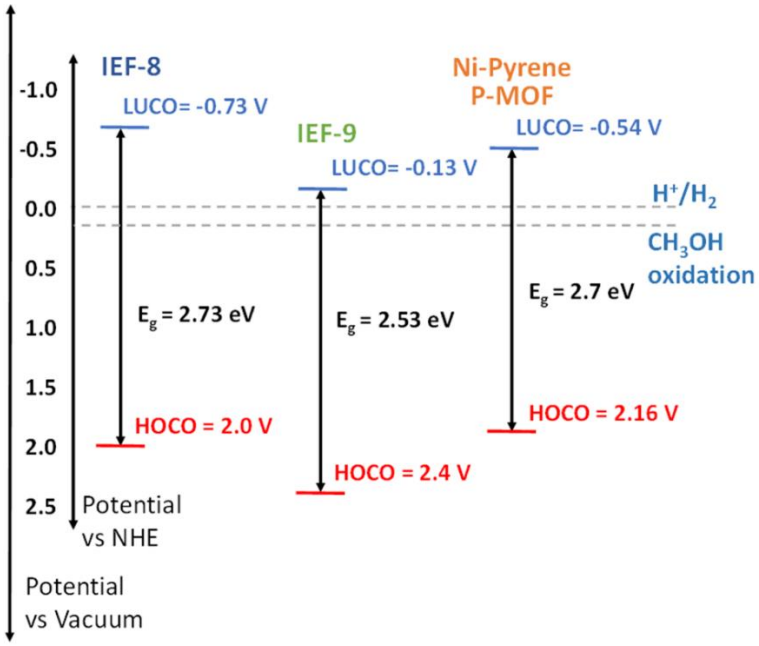

Figure 3. Energy level diagram of IEF-8, IEF-9 and Ni-Pyrene P-MOF.

Photocatalytic efficiency in HER

The photocatalytic activity of the novel Cu-based MOFs IEF-8 and IEF-9 was evaluated for HER. As shown in Figure 4a, IEF-8 exhibits the highest photocatalytic activity, achieving a hydrogen production of around 1800 $\mu mol \cdot g^{-1}$ after 22 h under UV-Vis irradiation. In comparison, IEF-9 presented a lower activity (740 $\mu mol \cdot g^{-1}$ after 22 h). Upon photocatalytic reaction, the structural integrity of IEF-8 and IEF-9 solids was kept, as evidenced by PXRD (Figure S29). Further evaluation of the chemical stability by monitoring the leaching of the copper to the reaction solution by ICP-OES revealed a higher robustness of the more active IEF-8 (<0.2 wt%) than the less active, IEF-9 (4.3 wt%).

When comparing both Cu-based P-MOFs, the higher hydrogen generation of IEF-8 *vs.* IEF-9 could be explained by different factors. On one hand, the higher reduction potential of IEF-8 when compared with IEF-9 (-0.73 *vs*. -0.13 V, respectively). In this sense, one could also suggest that

the different SBU should affect their photocatalytic activity. While IEF-8 presents pentacoordinate clusters (CuO_5 square-based pyramids, where Cu is at the base of the pyramid), IEF-9 structure is based on chains of hexacoordinate clusters (CuO_6 octahedra) connected to tetracoordinate clusters (square-planar CuO_4). This different coordination could influence the accessibility of the metal centers. Furthermore, although the number of coordinatively unsaturated metal sites (CUS) with Lewis acid character is the same *per* unit formula, IEF-8 presents one CUS for each Cu pentacoordinate Cu atom (CuO_5), and IEF-9 shows 2 CUS for each 2 Cu atoms of those that compose the octacoordinated clusters (CuO_6). Thus, due to the different nature of the SBUs, a different Lewis acid strength could be expected for the CUS in both structures and, consequently, different interactions during the catalytic reaction. On the other hand, the higher structural stability of IEF-8 (<0.2 vs. 4.0 % degradation) and the presence of a larger number of free water molecules in their structure (specifically, 4 *vs.* 3 water molecules *per* chemical formula in IEF-8 and IEF-9) could contribute also to the better catalytic water splitting performance. Note here that both MOFs present the same number of coordinated water molecules in their structures (2 water molecules *per* formula).

Considering the higher photocatalytic activity and stability of IEF-8, this solid was selected to further evaluate the heterogeneity of the reaction in presence of this catalyst. Thus, upon the removal of the IEF-8 catalyst from the HER reaction system, no hydrogen production was observed (Figure 4a, red line), confirming that the photocatalytic activity is truly heterogeneous.

In order to further compare the catalytic performances of IEF-8 with other photocatalysts, commercial copper oxide, the Ni-Pyrene P-MOF and the benchmarked Ti-based MOF photocatalyst MIL-125(Ti)-NH_2 were employed as photocatalyst under similar reaction conditions (22 h under UV-Vis irradiation). Commercial copper oxide and Ni-Pyrene P-MOF as controls

results in much lower HER respect to IEF-8 (391 and 929 *vs*. 1800 μmol·g^{-1}, respectively), evidencing the role of both the photoactive pyrene ligand as light harvesting unit (higher performance of IEF-8 and Ni-Pyrene P-MOF) and the influence of the nature of the redox properties of the transition metal (Cu^{2+} more efficient than Ni^{2+}). Considering that IEF-8 and Ni P-MOF have similar band gap values (~2.7 eV) and photostability based on XRD and ICP measurements (<0.3% degradation; Figure S28), the higher photoactivity of IEF-8 could be attributed to its more negative reduction potential of the Lowest Unoccupied Crystal Orbital (LUCO) level, having higher driving force to promote HER associated to the Cu cation. Interestingly, IEF-8 photocatalyst is 2.2 times more efficient than MIL-125(Ti)-NH_2 (1800 *vs.* 825 μmol·g^{-1}). Considering that these two MOFs have similar band gap values (~2.7 eV), the higher HER using the former could be associated to the more negative LUCO value of IEF-8 (-0.73 V) *vs.* MIL-125(Ti)-NH_2 (-0.65 eV).[48] Even further, although one should consider the complex comparison between studies using different conditions (type of lamp, irradiation, reaction times, concentration, sacrificial agents, use co-catalysts/sensitizers, cyclability, etc.), the activity of IEF-8 has been compared with other MOF photocatalysts (Table S5, reader is referred also to some recent reviews[30,49]). It seems that IEF-8 is one of the best photocatalysts in HER in absence of any co-catalysts/sensitizer, not only in the H_2 production but also in its cyclability.

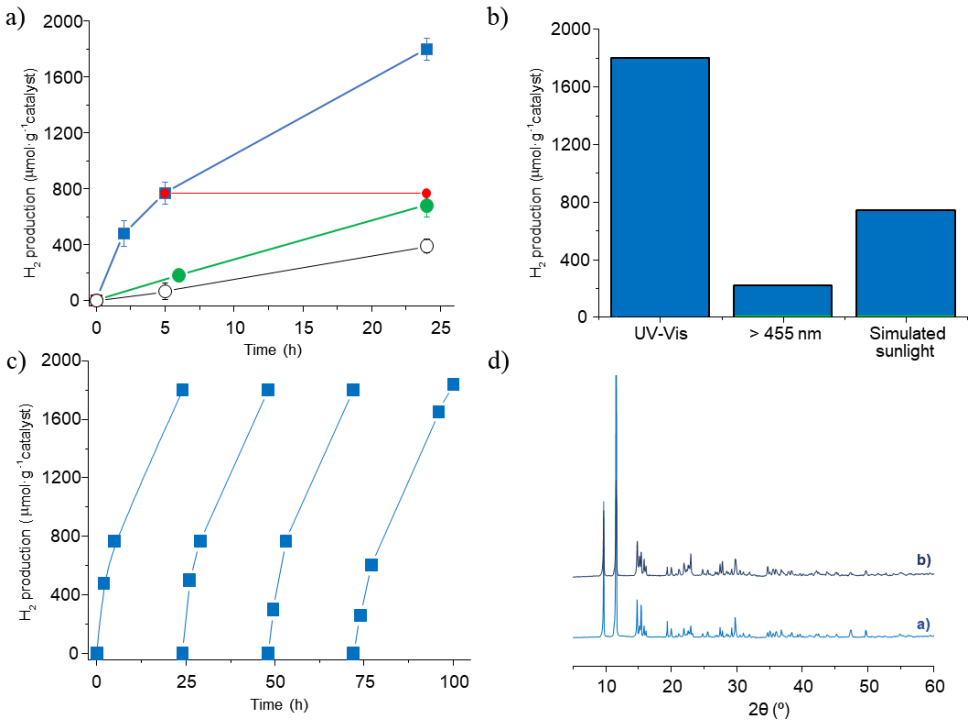

Figure 4. a) Photocatalytic HER using IEF-8 (■), IEF-9 (●) or commercial copper oxide (○) under UV-Vis light irradiation. The red line shows the photocatalytic HER upon removal of IEF-8 catalyst after 5 h during the first catalytic cycle (●). b) Influence of the irradiation source on the photocatalytic HER using IEF-8. c) IEF-8 reusability during the photocatalytic HER under UV-Vis irradiation. d) PXRD patterns of the fresh (a) and four-times used IEF-8 photocatalyst (b). Reaction conditions: Photocatalyst (10 mg), H_2O (15 mL), MeOH (5 mL), Hg-Xe lamp (150 W) output beam without filter or equipped or not with filters (AM 1.5 filter or $\lambda > 455$ nm) as indicated in each respective caption.

Besides, the activity of IEF-8 was also evaluated using different light sources (UV-Vis, >455 nm and simulated sunlight; Figure 4b), confirming its activity upon irradiation in all these wavelength regions. In this sense, although the produced hydrogen under more real conditions (*i.e.*

simulated sunlight) significantly decreases when compared with the obtained using UV-Vis irradiation (1800 *vs.* 743 $\mu mol \cdot g^{-1}$, this H_2 evolution value is still a high value in the current state of the art considering the absence of co-catalysts. As expected, the use of a cut-off filter that allows only irradiations with wavelengths higher than 455 nm results in the conditions with the lowest photocatalytic activity since the IEF-8 exhibits low absorption at these visible wavelengths (Figure S26a). Finally, IEF-8 also proved to be recyclable 4 cycles, retaining its photocatalytic activity (Figure 4c), preserving its crystalline structure (Figure 4d) and exhibiting the same functional groups than the fresh material as revealed by FT-IR (Figure S30). These results highlight the potential of developing novel P-MOF-based photocatalysts with improved photocatalytic activity for the HER without the need of a noble metal co-catalyst.

In order to further evaluate the ability of the IEF-8 to promote photoinduced reduction reactions, methyl viologen (MV^{2+}; E^0 = -0.44 V) was used as probe molecule.[50] It is well-known that the one-electron reduction of MV^{2+} results in the formation of its corresponding blue-colored $MV^{\bullet+}$ radical cation that can be usually observed and monitored by UV-Vis optical spectroscopy.[51] Figure 5a shows that IEF-8 was able to promote the one-electron reduction of MV^{2+} to $MV^{\bullet+}$ under UV-Vis irradiation. This observation indicates the occurrence of photoinduced charge separation when using IEF-8 as photocatalyst under UV-Vis irradiation. Further evidence to support this hypothesis was obtained by photocurrent measurements. The photocurrent response of the IEF-8 supported on an FTO support as a function of the polarization voltage during five light on/off 1 min cycles using acetonitrile as solvent and $NBuPF_6$ as electrolyte is depicted in Figure 5b. The presence of methanol during the measurements increased the photocurrent response, a fact that agrees with its role as a sacrificial electron donating agent that quenches the photogenerated holes and, thus, avoids the electron/hole pair recombination, proving the ability of IEF-8 as efficient photocatalyst.

EPR spectroscopy was used to monitor the change in Cu(II) environment and its concentration upon irradiation of the IEF-8 as a solid powder with UV-visible radiation. The results, presented in Figure S31a, show a decrease in the component at lower field and a shift in the position of the higher field component, as well as the appearance of a new peak. The decrease in the intensity of the low-field peak reflects a decrease in the population of Cu(II) becoming Cu(I) (EPR silent), while the shift in the position of the high-field component and the appearance of a new component indicates a change in the coordination of the remaining Cu(II) ions under steady-state irradiation. We propose that photogenerated Cu(I) species are responsible for the proton reduction to hydrogen atoms, two of which combine to form H_2. Additionally, the positive holes present on the organic ligands might act as active centers to oxidize methanol that is present as sacrificial electron donor (Figure S31b).

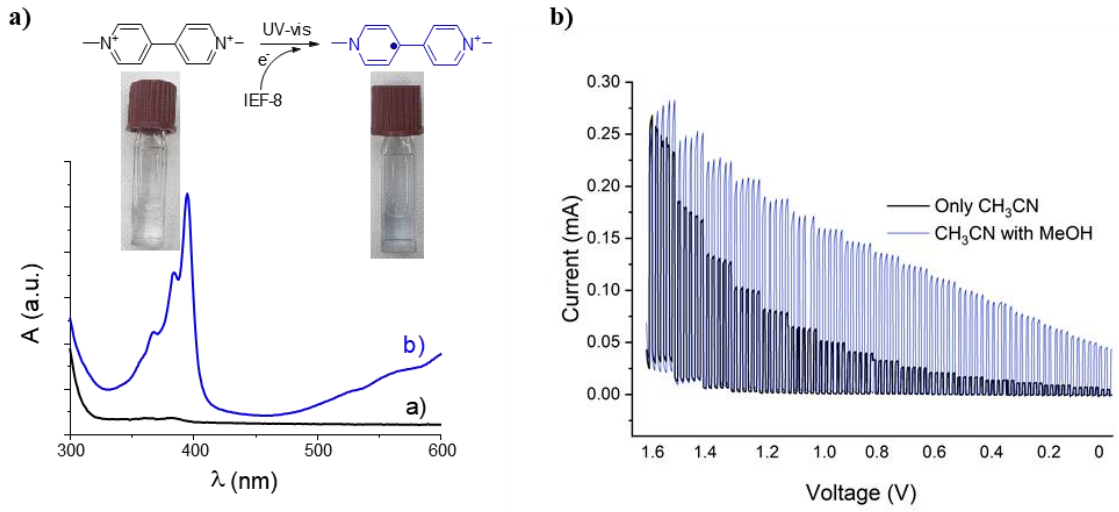

Figure 5. a) Observation of the photoinduced one-electron reduction reaction of MV^{2+} to $MV^{\bullet+}$, photographs of the MV^{2+} solution before (left side) and after the irradiation (right side and blue colored solution) in the presence of IEF-8 as photocatalyst. b) Photocurrent response of IEF-8 material supported on FTO electrode in acetonitrile (b1) or

acetonitrile/methanol (b2) solution upon electrode polarization during five light on/off cycles using a Hg-Xe lamp (150 W).

CONCLUSIONS

Two novel Cu-based P-MOF structures (branded as IEF-8 & 9) were hydrothermally synthesized using a photoactive tetraphosphonate pyrene derivate as ligand. These materials presented good thermal and chemical stability (organic solvents typically used in catalysis and hydrogen photogeneration). Their optoelectronic properties were assessed finding that both of them show promising features as photocatalysts (bandgap 2.7 eV). In particular, IEF-8 presented a higher catalytic efficiency producing 1800 $\mu mol \cdot g^{-1}$ after 22 h without co-catalyst, this value exceeding the benchmarked MIL-125(Ti)-NH_2 photocatalyst. Furthermore, the material presented a good reusability at least up to 4 cycles preserving its activity and structural integrity. This work paves the way to employ phosphonate MOFs not only for hydrogen generation but also in other catalytic reactions relevant in different societal and economically-key fields.

Supporting Information

The Supporting Information is available free of charge at (link here).

Snapshots from SEM, SC-XRD structures, Le Bail profile refinements, PXRD patterns, FTIR spectra, TGA, TV-XRD experiments, chemical stability tests, XPS data, CPS valence bands, UV-Vis diffuse spectra of the samples (PDF)

ACKNOWLEDGEMENT

Authors acknowledge the María de Maeztu IMDEA Energy Institute, the M-ERA-NET C-MOF-cell project and Retos Investigación MOFSEIDON project (PID2019-104228RB-I00 funded by MCIN/AEI/ 10.13039/501100011033 and by the European Union, MICIU-AEI/FEDER, UE) and

H2-MOF project (TED2021-132092B-C21 funded by MCIN/AEI/ 10.13039/501100011033 and by the European Union NextGenerationEU/PRTR). We thank “Comunidad de Madrid” and European Regional Development Fund-FEDER 2014-2020-OE REACT-UE 1 for their financial support to VIRMOF-CM project associated to R&D projects in response to COVID-19.

PRESENT ADDRESS

[#]**Pablo Salcedo-Abraira** – Nantes Université, Nantes, F-44000, France

[#]**Artem A. Babaryk** – University of Oviedo, Oviedo, 33006, Spain

[#]**David Tilve-Martínez** – Université de Bordeaux, Pessac, 33600, France

REFERENCES

(1) Pearson, R. G. Hard and Soft Acids and Bases. J. Am. Chem. Soc. 1963, 85 (22), 3533–3539. https://doi.org/10.1021/ja00905a001.

(2) Mysore Ramesha, B.; Meynen, V. Advances and Challenges in the Creation of Porous Metal Phosphonates. Materials 2020, 13 (23), 5366. https://doi.org/10.3390/ma13235366.

(3) Gagnon, K. J.; Perry, H. P.; Clearfield, A. Conventional and Unconventional Metal–Organic Frameworks Based on Phosphonate Ligands: MOFs and UMOFs. Chem. Rev. 2012, 112 (2), 1034–1054. https://doi.org/10.1021/cr2002257.

(4) Tholen, P.; Zorlu, Y.; Beckmann, J.; Yücesan, G. Probing Isoreticular Expansions in Phosphonate MOFs and Their Applications. European Journal of Inorganic Chemistry 2020, 2020 (17), 1542–1554. https://doi.org/10.1002/ejic.201901291.

(5) Begum, S.; Horike, S.; Kitagawa, S.; Krautscheid, H. Water Stable Triazolyl Phosphonate MOFs: Steep Water Uptake and Facile Regeneration. Dalton Trans. 2015, 44 (43), 18727–18730. https://doi.org/10.1039/C5DT02651B.

(6) Kong, Z.; Niu, Z.; He, L.; Chen, Q.; Zhou, L.; Cheng, Y.; Guan, Q. In Situ Analysis of the Adsorption Behaviors of CO2 on the Surface of MIL-91(Al). New J. Chem. 2018, 42 (20), 16985–16991. https://doi.org/10.1039/C8NJ03833C.

(7) Medikonda, P.; Pilli, R.; Sastri, C. V.; Gumma, S. Adsorption of Gases on Small–Pore Aluminum Bisphosphonate MOF MIL–91(Al). J Chem Sci 2021, 133 (4), 100. https://doi.org/10.1007/s12039-021-01964-9.

(8) Vilela, S. M. F.; Navarro, J. A. R.; Barbosa, P.; Mendes, R. F.; Pérez-Sánchez, G.; Nowell, H.; Ananias, D.; Figueiredo, F.; Gomes, J. R. B.; Tomé, J. P. C.; Paz, F. A. A. Multifunctionality in an Ion-Exchanged Porous Metal–Organic Framework. J. Am. Chem. Soc. 2021, 143 (3), 1365–1376. https://doi.org/10.1021/jacs.0c10421.

(9) Nistor, M. A.; Muntean, S. G.; Maranescu, B.; Visa, A. Phosphonate Metal–Organic Frameworks Used as Dye Removal Materials from Wastewaters. Applied Organometallic Chemistry 2020, 34 (11), e5939. https://doi.org/10.1002/aoc.5939.

(10) Chakraborty, D.; Musib, D.; Saha, R.; Das, A.; Raza, M. K.; Ramu, V.; Chongdar, S.; Sarkar, K.; Bhaumik, A. Highly Stable Tetradentate Phosphonate-Based Green Fluorescent Cu-MOF for Anticancer Therapy and Antibacterial Activity. Materials Today Chemistry 2022, 24, 100882. https://doi.org/10.1016/j.mtchem.2022.100882.

(11) Lian, X.; Yan, B. Phosphonate MOFs Composite as Off–On Fluorescent Sensor for Detecting Purine Metabolite Uric Acid and Diagnosing Hyperuricuria. Inorg. Chem. 2017, 56 (12), 6802–6808. https://doi.org/10.1021/acs.inorgchem.6b03009.

(12) Vassaki, M.; Papathanasiou, K. E.; Hadjicharalambous, C.; Chandrinou, D.; Turhanen, P.; Choquesillo-Lazarte, D.; Demadis, K. D. Self-Sacrificial MOFs for Ultra-Long Controlled Release of Bisphosphonate Anti-Osteoporotic Drugs. Chem. Commun. 2020, 56 (38), 5166–5169. https://doi.org/10.1039/D0CC00439A.

(13) Chen, X.; Peng, Y.; Han, X.; Liu, Y.; Lin, X.; Cui, Y. Sixteen Isostructural Phosphonate Metal-Organic Frameworks with Controlled Lewis Acidity and Chemical Stability for Asymmetric Catalysis. Nat Commun 2017, 8 (1), 2171. https://doi.org/10.1038/s41467-017-02335-0.

(14) Li, F.; Jiang, S.; Zhu, T.; Wang, Y.; Huang, T.; Li, C. Organodiphosphonate Metal-Organic Frameworks Derived Ni-P@C Catalyst for Hydrogenation of Furfural. ChemistrySelect 2020, 5 (7), 2271–2278. https://doi.org/10.1002/slct.201902827.

(15) Salcedo-Abraira, P.; Vilela, S. M. F.; Babaryk, A. A.; Cabrero-Antonino, M.; Gregorio, P.; Salles, F.; Navalón, S.; García, H.; Horcajada, P. Nickel Phosphonate MOF as Efficient Water Splitting Photocatalyst. Nano Res. 2021, 14 (2), 450–457. https://doi.org/10.1007/s12274-020-3056-6.

(16) Zhu, Y.-P.; Yin, J.; Abou-Hamad, E.; Liu, X.; Chen, W.; Yao, T.; Mohammed, O. F.; Alshareef, H. N. Highly Stable Phosphonate-Based MOFs with Engineered Bandgaps for Efficient Photocatalytic Hydrogen Production. Advanced Materials 2020, 32 (16), 1906368. https://doi.org/10.1002/adma.201906368.

(17) Levenson, D. A.; Zhang, J.; Gelfand, B. S.; Kammampata, S. P.; Thangadurai, V.; Shimizu, G. K. H. Particle Size Dependence of Proton Conduction in a Cationic Lanthanum Phosphonate MOF. Dalton Trans. 2020, 49 (13), 4022–4029. https://doi.org/10.1039/C9DT04229F.

(18) Vilela, S. M. F.; Salcedo-Abraira, P.; Gómez-Peña, A.; Trens, P.; Várez, A.; Salles, F.; Horcajada, P. Proton Conductive Zr-Phosphonate UPG-1—Aminoacid Insertion as Proton Carrier Stabilizer. Molecules 2020, 25 (15), 3519. https://doi.org/10.3390/molecules25153519.

(19) Salcedo-Abraira, P.; Vilela, S. M. F.; Ureña, N.; Salles, F.; Várez, A.; Horcajada, P. Ion-Exchanged UPG-1 as Potential Electrolyte for Fuel Cells. Inorg. Chem. 2021, 60 (16), 11803–11812. https://doi.org/10.1021/acs.inorgchem.1c00800.

(20) Chakraborty, D.; Chowdhury, A.; Chandra, M.; Jana, R.; Shyamal, S.; Bhunia, M. K.; Chandra, D.; Hara, M.; Pradhan, D.; Datta, A.; Bhaumik, A. Novel Tetradentate Phosphonate Ligand Based Bioinspired Co-Metal–Organic Frameworks: Robust Electrocatalyst for the Hydrogen Evolution Reaction in Different Mediums. Crystal Growth & Design 2021, 21 (5), 2614–2623. https://doi.org/10.1021/acs.cgd.0c01275.

(21) Gao, J.; Huang, Q.; Wu, Y.; Lan, Y.-Q.; Chen, B. Metal–Organic Frameworks for Photo/Electrocatalysis. Advanced Energy and Sustainability Research 2021, 2 (8), 2100033. https://doi.org/10.1002/aesr.202100033.

(22) Wen, X.; Guan, J. Recent Progress on MOF-Derived Electrocatalysts for Hydrogen Evolution Reaction. Applied Materials Today 2019, 16, 146–168. https://doi.org/10.1016/j.apmt.2019.05.013.

(23) Wang, P.; Zhang, X.; Shi, R.; Zhao, J.; Yuan, Z.; Zhang, T. Light-Driven Hydrogen Production from Steam Methane Reforming via Bimetallic PdNi Catalysts Derived from Layered Double Hydroxide Nanosheets. Energy Fuels 2022, 36 (19), 11627–11635. https://doi.org/10.1021/acs.energyfuels.2c01349.

(24) Smiljanic, M.; Rakocevic, Z.; Maksic, A.; Strbac, S. Hydrogen Evolution Reaction on Platinum Catalyzed by Palladium and Rhodium Nanoislands. Electrochimica Acta 2014, 117, 336–343. https://doi.org/10.1016/j.electacta.2013.11.142.

(25) Ke, G.-L.; Jia, B.; He, H.-C.; Zhou, Y.; Zhou, M. State-of-the-Art Advancements of Transition Metal Oxides as Photoelectrode Materials for Solar Water Splitting. Rare Met. 2022, 41 (7), 2370–2386. https://doi.org/10.1007/s12598-022-01968-5.

(26) Zahra, R.; Pervaiz, E.; Yang, M.; Rabi, O.; Saleem, Z.; Ali, M.; Farrukh, S. A Review on Nickel Cobalt Sulphide and Their Hybrids: Earth Abundant, PH Stable Electro-Catalyst for Hydrogen Evolution Reaction. International Journal of Hydrogen Energy 2020, 45 (46), 24518–24543. https://doi.org/10.1016/j.ijhydene.2020.06.236.

(27) Li, Z.; Feng, H.; Song, M.; He, C.; Zhuang, W.; Tian, L. Advances in CoP Electrocatalysts for Water Splitting. Materials Today Energy 2021, 20, 100698. https://doi.org/10.1016/j.mtener.2021.100698.

(28) Lin, H.; Xu, Y.; Wang, B.; Li, D.-S.; Zhou, T.; Zhang, J. Postsynthetic Modification of Metal−Organic Frameworks for Photocatalytic Applications. Small Structures 2022, 3 (5), 2100176. https://doi.org/10.1002/sstr.202100176.

(29) Li, X.; Wang, Z.; Wang, L. Metal–Organic Framework-Based Materials for Solar Water Splitting. Small Science 2021, 1 (5), 2000074. https://doi.org/10.1002/smsc.202000074.

(30) Zhang, K.; Hu, H.; Shi, L.; Jia, B.; Huang, H.; Han, X.; Sun, X.; Ma, T. Strategies for Optimizing the Photocatalytic Water-Splitting Performance of Metal–Organic Framework-Based Materials. Small Science 2021, 1 (12), 2100060. https://doi.org/10.1002/smsc.202100060.

(31) Nguyen, H. L. Metal–Organic Frameworks for Photocatalytic Water Splitting. Solar RRL 2021, 5 (7), 2100198. https://doi.org/10.1002/solr.202100198.

(32) Luo, H.; Zeng, Z.; Zeng, G.; Zhang, C.; Xiao, R.; Huang, D.; Lai, C.; Cheng, M.; Wang, W.; Xiong, W.; Yang, Y.; Qin, L.; Zhou, C.; Wang, H.; Zhou, Y.; Tian, S. Recent Progress on Metal-Organic Frameworks Based- and Derived-Photocatalysts for Water Splitting. Chemical Engineering Journal 2020, 383, 123196. https://doi.org/10.1016/j.cej.2019.123196.

(33) Pelin Kinik, F.; Ortega-Guerrero, A.; Ongari, D.; P. Ireland, C.; Smit, B. Pyrene-Based Metal Organic Frameworks: From Synthesis to Applications. Chemical Society Reviews 2021, 50 (5), 3143–3177. https://doi.org/10.1039/D0CS00424C.

(34) Firmino, A. D. G.; Mendes, R. F.; Ananias, D.; Figueira, F.; Tomé, J. P. C.; Rocha, J.; Almeida Paz, F. A. Pyrene Tetraphosphonate-Based Metal-Organic Framework: Structure and Photoluminescence. European Journal of Inorganic Chemistry 2020, 2020 (37), 3565–3572. https://doi.org/10.1002/ejic.202000726.

(35) Taylor, J. M.; Vaidhyanathan, R.; Iremonger, S. S.; Shimizu, G. K. H. Enhancing Water Stability of Metal–Organic Frameworks via Phosphonate Monoester Linkers. J. Am. Chem. Soc. 2012, 134 (35), 14338–14340. https://doi.org/10.1021/ja306812r.

(36) Gao, C.-Y.; Yang, Y.; Xu, N.; Liu, J.; Duan, L.; Chen, X.; Bao, M. A Ni II Phosphonate as an Efficient Catalyst for the Synthesis of Cyclic Carbonate under Ambient Conditions. Crystal Growth & Design 2021, 21 (3), 1413–1417. https://doi.org/10.1021/acs.cgd.0c01628.

(37) Siavash Moakhar, R.; Hosseini-Hosseinabad, S. M.; Masudy-Panah, S.; Seza, A.; Jalali, M.; Fallah-Arani, H.; Dabir, F.; Gholipour, S.; Abdi, Y.; Bagheri-Hariri, M.; Riahi-Noori, N.; Lim, Y.-F.; Hagfeldt, A.; Saliba, M. Photoelectrochemical Water-Splitting Using CuO-Based Electrodes for Hydrogen Production: A Review. Advanced Materials 2021, 33 (33), 2007285. https://doi.org/10.1002/adma.202007285.

(38) Wang, J.; Cherevan, A. S.; Hannecart, C.; Naghdi, S.; Nandan, S. P.; Gupta, T.; Eder, D. Ti-Based MOFs: New Insights on the Impact of Ligand Composition and Hole Scavengers on Stability, Charge Separation and Photocatalytic Hydrogen Evolution. Applied Catalysis B: Environmental 2021, 283, 119626. https://doi.org/10.1016/j.apcatb.2020.119626.

(39) Sheldrick, G. M. SHELXT – Integrated Space-Group and Crystal-Structure Determination. Acta Crystallographica Section A Foundations and Advances 2015, 71 (1), 3–8. https://doi.org/10.1107/S2053273314026370.

(40) Sheldrick, G. M. Crystal Structure Refinement with SHELXL. Acta Crystallographica Section C Structural Chemistry 2015, 71 (1), 3–8. https://doi.org/10.1107/S2053229614024218.

(41) Rodríguez-Carvajal, J. Recent Advances in Magnetic Structure Determination by Neutron Powder Diffraction. Physica B: Condensed Matter 1993, 192 (1–2), 55–69. https://doi.org/10.1016/0921-4526(93)90108-I.

(42) Stock, N. High-Throughput Investigations Employing Solvothermal Syntheses. Microporous and Mesoporous Materials 2010, 129 (3), 287–295. https://doi.org/10.1016/j.micromeso.2009.06.007.

(43) Halcrow, M. A. Jahn–Teller Distortions in Transition Metal Compounds, and Their Importance in Functional Molecular and Inorganic Materials. Chem. Soc. Rev. 2013, 42 (4), 1784–1795. https://doi.org/10.1039/C2CS35253B.

(44) Akgul, F. A.; Akgul, G.; Yildirim, N.; Unalan, H. E.; Turan, R. Influence of Thermal Annealing on Microstructural, Morphological, Optical Properties and Surface Electronic Structure of Copper Oxide Thin Films. Materials Chemistry and Physics 2014, 147 (3), 987–995. https://doi.org/10.1016/j.matchemphys.2014.06.047.

(45) Cendula, P.; Tilley, S. D.; Gimenez, S.; Bisquert, J.; Schmid, M.; Grätzel, M.; Schumacher, J. O. Calculation of the Energy Band Diagram of a Photoelectrochemical Water Splitting Cell. J. Phys. Chem. C 2014, 118 (51), 29599–29607. https://doi.org/10.1021/jp509719d.

(46) Xue, Z.; Liu, K.; Liu, Q.; Li, Y.; Li, M.; Su, C.-Y.; Ogiwara, N.; Kobayashi, H.; Kitagawa, H.; Liu, M.; Li, G. Missing-Linker Metal-Organic Frameworks for Oxygen Evolution Reaction. Nat Commun 2019, 10 (1), 5048. https://doi.org/10.1038/s41467-019-13051-2.

(47) Gikonyo, B.; Montero-Lanzuela, E.; Baldovi, H. G.; De, S.; Journet, C.; Devic, T.; Guillou, N.; Tiana, D.; Navalon, S.; Fateeva, A. Mixed-Metal Zr/Ti MIL-173 Porphyrinic Metal–Organic Frameworks as Efficient Photocatalysts towards Solar-Driven Overall Water Splitting. J. Mater. Chem. A 2022, 10 (46), 24938–24950. https://doi.org/10.1039/D2TA06652A.

(48) Zhao, Y.; Cai, W.; Chen, J.; Miao, Y.; Bu, Y. A Highly Efficient Composite Catalyst Constructed From NH2-MIL-125(Ti) and Reduced Graphene Oxide for CO2 Photoreduction. Frontiers in Chemistry 2019, 7, 789. https://doi.org/10.3389/fchem.2019.00789.

(49) Navalón, S.; Dhakshinamoorthy, A.; Álvaro, M.; Ferrer, B.; García, H. Metal–Organic Frameworks as Photocatalysts for Solar-Driven Overall Water Splitting. Chem. Rev. 2022, 123 (1), 445–490. https://doi.org/10.1021/acs.chemrev.2c00460.

(50) Cabrero-Antonino, M.; Albero, J.; García-Vallés, C.; Álvaro, M.; Navalón, S.; García, H. Plasma-Induced Defects Enhance the Visible-Light Photocatalytic Activity of MIL-125(Ti)-NH2 for Overall Water Splitting. Chemistry - A European Journal 2020, 26 (67), 15682–15689. https://doi.org/10.1002/chem.202003763.

(51) Ebbesen, T. W.; Ferraudi, G. Photochemistry of Methyl Viologen in Aqueous and Methanolic Solutions. Journal of Physical Chemistry 1983, 87 (19), 3717–3721. https://doi.org/10.1021/j100242a028.